J|A|C|S
ARTICLES
Published on Web 03/29/2002

Theoretical Study on the Stability of *N*-Glycosyl Bonds: Why Does N7-Platination Not Promote Depurination?

Mu-Hyun Baik,[†] Richard A. Friesner,*[,†] and Stephen J. Lippard*[,‡]

Contribution from the Department of Chemistry, Columbia University, New York, New York 10027, and Department of Chemistry, Massachusetts Institute of Technology, Cambridge, Massachusetts 02139

Received November 21, 2001

Abstract: The depurination reaction of guanosine, protonated or modified with cisplatin at the N7 position, has been studied by density functional theory (DFT), coupled with a continuum treatment of solvation. Protonation accelerates the depurination reaction whereas N7-platination, the initial product of cisplatin binding to DNA, does not. The computed reaction energy profiles demonstrate that N7-platination has only a minor effect on the energetics of the transition state, whereas protonation lowers it by ~10 kcal mol^{-1}. The orbitals involved in N7-Pt/H bonding are examined, and electronic differences between the two substituted guanines are identified. Natural bond orbital analysis, fragment orbital analysis, and extended transition-state theory reveal how the electronically different substituents at the N7 position control the stability of the N9−C1′ bond. The detailed description of the electronic structure of the N7-substituted guanosines and the computational protocol developed to obtain a realistic model for these systems not only explain a longstanding enigma but also provide guidelines for further studies toward understanding the interactions of cisplatin with DNA.

Introduction

Depurination, the cleavage of the *N*-glycosyl bond between a purine base and its deoxyribose sugar moiety, is a common form of DNA damage and one of the main mechanisms responsible for the susceptibility of DNA to hydrolysis.[1] Both acidic conditions[2] and alkylating agents[3] accelerate depurination by electrophilic attack at the most reactive nucleophile on DNA, the N7 position of guanine. Recently, the chemistry of base-excision glycosylases has been reviewed.[4a] These enzymes utilize the intrinsic instability of the *N*-glycosyl bond to perform DNA repair. Similar destabilization mechanisms are operative in DNA strand scission processes induced by oxidative modifications.[4b] An intriguing example of this chemistry is the cytotoxic mechanism of Ricin Toxin A-chain (RTA), which is a consequence of its ability to catalyze the depurination of DNA.[5] Acid-catalyzed depurination proceeds via a fast protonation step followed by unimolecular rate-limiting cleavage of the C−N bond (eq 1).[6] A few theoretical studies of the hydrolysis of guanosine and adenosine have appeared in the literature,[7] identifying local charge and steric effects as likely contributors to the instability of the *N*-glycosyl bond; however, these studies have not provided a conclusive picture of the electronic details dictating the reaction profile.

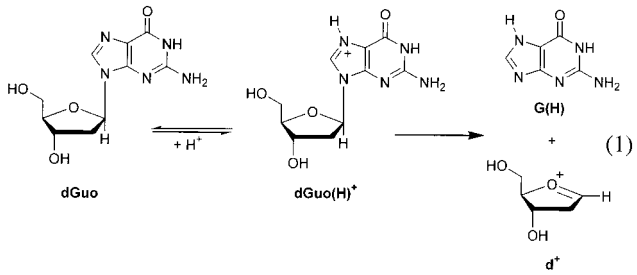

(1)

The N7 position of guanine is also the preferred binding site for *cis*-$[Pt(NH_3)_2Cl(H_2O)]^+$, the active form of the widely used anticancer drug cisplatin (*cis*-$[Pt(NH_3)_2Cl_2]$, *cis*-DDP, or *cis*-diamminedichloroplatinum(II)).[8] The major cisplatin−DNA adducts comprise 1,2-intrastrand cross-links between adjacent guanine bases[9,10] with Pt−N7 bonds that structurally distort the DNA duplex[10a,b] and ultimately lead to the genotoxicity and antitumor activity. The necessary first step in this process,

* To whom correspondence should be addressed.
[†] Columbia University.
[‡] Massachusetts Institute of Technology.

(1) (a) Lindahl, T. *Prog. Nucleic Acid Res. Mol. Biol.* **1979**, *22*, 135−192. (b) Suzuki, T.; Ohsumi, S.; Makino. K. *Nucleic Acids Res.* **1994**, *22*, 4997−5003. (c) Lindahl, T. *Nature* **1993**, *362*, 709−715.
(2) Roger, M.; Hotchkiss, R. *Proc. Natl. Acad. Sci. U.S.A.* **1961**, *47*, 654−669.
(3) Tamm, C.; Shapiro, H. S.; Lipshitz, R.; Chargaff, E. *J. Biol. Chem.* **1953**, *203*, 673−688.
(4) (a) David, S. S.; Williams, S. D. *Chem. Rev.* **1998**, *98*, 1221−1261. (b) Burrows, C. J.; Muller, J. G. *Chem. Rev.* **1998**, *98*, 1109−1151.
(5) Chen, X.-Y.; Berti, P. J.; Schramm, V. L. *J. Am. Chem. Soc.* **2000**, *122*, 6527−6534.
(6) (a) Zoltewicz, J. A.; Clark, D. F.; Sharpless, T. W.; Grahe, G. *J. Am. Chem. Soc.* **1970**, *92*, 1741−1750. (b) Garrett, E. R.; Mehta, P. J. *J. Am. Chem. Soc.* **1972**, *94*, 8532−8537. (c) Garrett, E. R.; Mehta, P. J. *J. Am. Chem. Soc.* **1972**, *94*, 8542−8547. (d) Yanagawa, H.; Ogawa, Y.; Ueno, M. *J. Biol. Chem.* **1992**, *267*, 13320−13326. (e) Li, X.-Y.; McClure, W. R. *J. Biol. Chem.* **1998**, *273*, 23558−23566.
(7) (a) Cavalieri, E. L.; Vauthier, E. C.; Cosse-Barbi, A.; Fliszar, S. *Theor. Chem. Acc.* **2000**, *104*, 235−239. (b) Hotokka, M.; Lönnberg, H. *J. Mol. Struct. (THEOCHEM)* **1996**, *363*, 191−201.
(8) Jamieson, E. R.; Lippard, S. J. *Chem. Rev.* **1999**, *99*, 2467−2498.

formation of a monofunctional Pt−N7 adduct,[10c,d] does not increase the rate of depurination,[11] although the characteristics so far recognized for promoting depurination, such as excess positive charge, to afford a better leaving group for the unimolecular reaction, and steric bulk,[7] are clearly present (eq 2). This nonintuitive lack of reactivity has been widely acknowledged for nearly three decades, but a satisfactory explanation has thus far remained elusive. Understanding the electronic details that alter the stability of the *N*-glycosyl bond upon chemical modification is thus important for many reasons. Here, we address the lack of reactivity displayed by the monofunctional adduct of cisplatin with a DNA fragment and investigate for comparison purposes how the proton interacts with guanosine. Recently, a few computational studies of cisplatin−DNA adducts have appeared in the literature,[12] but the present report is the first thorough electronic structure investigation of the depurination reaction using a realistic model that accounts for both solvation and entropy changes. We apply an array of theoretical computation and analysis methods based on density functional theory (DFT)[13] to examine the depurination reaction of deoxyguanosine (dGuo), N7-protonated deoxyguanosine (dGuo(H)$^+$), and N7-platinated deoxyguanosine (dGuo(Pt)$^+$).

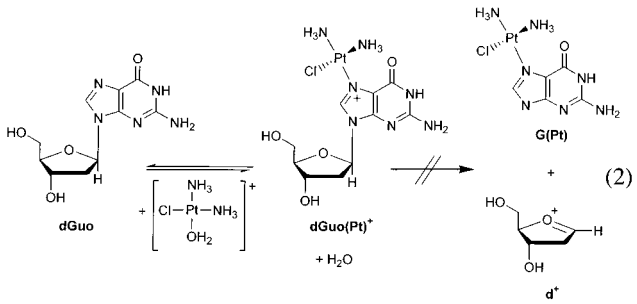

Computational Details and Theoretical Methods

All calculations were carried out using density functional theory as implemented in the Jaguar 4.1 suite[14] of ab initio quantum chemistry programs and the Amsterdam Density Functional 2000 package (ADF).[15] Geometries were optimized using Jaguar at the B3LYP[16]/6-31G** level, and for platinum the Los Alamos LACVP** basis[17] that includes relativistic effective core potentials was used. The energies were reevaluated by single point calculations at each optimized geometry using Dunning's[18] correlation consistent triple-ζ basis set cc-pVTZ(-f)++ with two sets of diffuse functions added to the standard double set of polarization functions. For platinum we applied a modified version of LACVP**, designated as LACV3P**++, where the exponents were decontracted to match the effective core potential with the triple-ζ quality basis, also with additional diffuse functions.[19] Vibrational frequency calculation results based on analytical second derivatives at the B3LYP/6-31G** level of theory were used to confirm proper convergence to local minima and to derive the zero-point energy (ZPE) and entropy corrections at room temperature. We neglect all electronic contributions to the thermal energy corrections. Solvation energies were evaluated by a self-consistent reaction field (SCRF) approach,[20] based on accurate numerical solutions of the Poisson−Boltzmann equation.[21] In the results reported below, solvation calculations were carried out at the gas-phase geometry using the cc-pVTZ(-f)++ basis and employing a dielectric constant of $\epsilon = 80.37$ for water.[22] Natural bond orbital (NBO) analyses were carried out using the Jaguar/B3LYP/6-31G** wave functions in Weinhold's NBO 4.0 package.[23] Additional single point calculations on the Jaguar-optimized structures were carried out using ADF to obtain fragment wave functions and to calculate energy decompositions according to the extended transition state (ETS) theory derived and implemented in ADF by Ziegler and Rauk.[24] In these calculations, a double-ζ STO basis set is utilized, with one set of polarization functions as provided in the ADF package (Basis Set III—frozen core), together with the BLYP functional.[16b,d] Relativistic effects on Pt are included using the "zero-

(9) den Hartog, J. H. J.; Altona, C.; van der Marel, G. A.; Reedijk, J. *Eur. J. Biochem.* **1985**, *147*, 371−379.
(10) (a) Sherman, S. E.; Gibson, D.; Wang, A. H.-J.; Lippard, S. J. *Science* **1985**, *230*, 412−417. (b) Sherman, S. E.; Gibson, D.; Wang, A. H.-J.; Lippard, S. J. *J. Am. Chem. Soc.* **1988**, *110*, 7368−7381. (c) Fichtinger-Schepman, A. M. J.; van der Veer, J. L.; den Hartog, J. H. J.; Lohman, P. H. M.; Reedijk, J. *Biochemistry* **1985**, *24*, 707−713. (d) Wing, R. M.; Pjura, P.; Drew, H. R.; Dickerson, R. E. *EMBO J.* **1984**, *3*, 1201−1206. (e) Gelasco, A.; Lippard, S. J. *Biochemistry* **1998**, *37*, 9230−9239.
(11) Johnson, N. P.; Macquet, J. P.; Wiebers, J. L.; Monsarrat, B. *Nucleic Acids Res.* **1982**, *10*, 5255−5271.
(12) (a) Carloni, P.; Sprik, M.; Andreoni, W. *J. Phys. Chem. B* **2000**, *104*, 823−835. (b) Carloni, P.; Andreoni, W. *J. Phys. Chem.* **1996**, *100*, 17797−17800. (c) Carloni, P.; Andreoni, W.; Hutter, J.; Curioni, A.; Giannozzi, P.; Parrinello, M. *Chem. Phys. Lett.* **1995**, *234*, 50−56. (d) Tornaghi, E.; Andreoni, W.; Carloni, P.; Hutter, J.; Parrinello, M. *Chem. Phys. Lett.* **1995**, *246*, 469−474. (e) Zhang, Y.; Guo, Z.; You, X.-Z. *J. Am. Chem. Soc.* **2001**, *123*, 9378−9387. (f) Sponer, J. E.; Leszczynski, J.; Glahe, F.; Lippert, B.; Sponer, J. *Inorg. Chem.* **2001**, *40*, 3269−3278. (g) Burda, J. V.; Sponer, J.; Leszczynski, J. *J. Biol. Inorg. Chem.* **2000**, *5*, 178−188.
(13) (a) Parr, R. G.; Yang, W. *Density Functional Theory of Atoms and Molecules*; Oxford University Press: New York, 1989. (b) Ziegler, T. *Chem. Rev.* **1991**, *91*, 651−667.
(14) (a) *Jaguar 4.1*; Schrödinger, Inc.: Portland, OR, 2000. (b) All orbital plots, both Jaguar and ADF orbitals, are prepared using a modified version of Molden 3.7: Schaftenaar, G.; Noordik, J. H. *J. Comput.-Aid. Mol. Des.* **2000**, *14*, 123−134.
(15) (a) Baerends, E. J.; Bérces, A.; Bo, C.; Boerrigter, P. M.; Cavallo, L.; Deng, L.; Dickson, R. M.; Ellis, D. E.; Fan, L.; Fischer, T. H.; Fonseca Guerra, C.; van Gisbergen, S. J. A.; Groeneveld, J. A.; Gritsenko, O. V.; Harris, F. E.; van den Hoek, P.; Jacobsen, H.; van Kessel, G.; Kootstra, F.; van Lenthe, E.; Osinga, V. P.; Philipsen, P. H. T.; Post, D.; Pye, C. C.; Ravenek, W.; Ros, P.; Schipper, P. R. T.; Schreckenbach, G.; Snijders, J. G.; Sola, M.; Swerhone, D.; te Velde, G.; Vernooijs, P.; Versluis, L.; Visser, O.; van Wezenbeek, E.; Wiesenekker, G.; Wolff, S. K.; Woo, T. K.; Ziegler, T. *ADF 2000.02*. (b) Fonseca Guerra, C.; Snijders, J. G.; te Velde, G.; Baerends, E. J. *Theor. Chem. Acc.* **1998**, *99*, 391−403.
(16) (a) Slater, J. C. *Quantum Theory of Molecules and Solids, Vol. 4: The Self-Consistent Field for Molecules and Solids*; McGraw-Hill: New York, 1974. (b) Becke, A. D. *Phys. Rev. A* **1988**, *38*, 3098−3100. (c) Vosko, S. H.; Wilk, L.; Nusair, M. *Can. J. Phys.* **1980**, *58*, 1200−1211. (d) Lee, C.; Yang, W.; Parr, R. G. *Phys. Rev. B* **1988**, *37*, 785−789. (e) Becke, A. D. *J. Chem. Phys.* **1993**, *98*, 5648−5652.
(17) (a) Hay, P. J.; Wadt, W. R. *J. Chem. Phys.* **1985**, *82*, 270−283. (b) Wadt, W. R.; Hay, P. J. *J. Chem. Phys.* **1985**, *82*, 284−298. (c) Hay, P. J.; Wadt, W. R. *J. Chem. Phys.* **1985**, *82*, 299−310.
(18) Dunning, T. H. *J. Chem. Phys.* **1989**, *90*, 1007−1023.
(19) To avoid numerical instabilities encountered for some transition metal containing systems of this size (Baik, M.-H.; Friesner, R. A. unpublished results) in combination with the highly diffuse basis, a modified version of the standard ultrafine grid provided in the Jaguar package was employed that enhances the numerical resolution for long-range interaction evaluations in each SCF cycle.
(20) For a review of continuum solvation models, see, for example: (a) Tomasi, J.; Persico, M. *Chem. Rev.* **1994**, *94*, 2027−2094. (b) Cramer, C. J.; Truhlar, D. G. In *Solvent Effects and Chemical Reactivity*; Tapia, O., Bertran, J., Eds.; Kluwer: Dordrecht, The Netherlands, 1996; pp 1−80.
(21) (a) Tannor, D. J.; Marten, B.; Murphy, R. B.; Friesner, R. A.; Sitkoff, D.; Nicholls, A.; Ringnalda, M. N.; Goddard, W. A., III; Honig, B. *J. Am. Chem. Soc.* **1994**, *116*, 11875−11882. (b) Marten, B.; Kim, K.; Cortis, C.; Friesner, R. A.; Murphy R. B.; Ringnalda, M. N.; Sitkoff, D.; Honig, B. *J. Phys. Chem.* **1996**, *100*, 11775−11788.
(22) We considered recomputing the geometry with the SCRF potential applied self-consistently but decided, after some experimentation, to neglect structural relaxation due to the SCRF potential and use the solvation energy computed at the optimized gas-phase geometries. This approach provides a reasonable compromise between computational cost and model sophistication. More details on the solvation energy calculations are given as Supporting Information.
(23) (a) Glendening, E. D.; Badenhoop, J. K.; Reed, A. E.; Carpenter, J. E.; Weinhold, F. *NBO 4.M*; Theoretical Chemistry Institute, University of Wisconsin: Madison, WI, 1999. (b) Unrestricted wave functions gave rise to inconsistent and obviously wrong NBO results, most likely because of a purely technical problem of the Jaguar/NBO interface. The continuum solvent-corrected wave functions also gave inconsistent results. The NBO calculations were therefore performed with restricted spin wave functions in the gas phase. All other calculations employ the unrestricted spin formalism.
(24) (a) Ziegler, T.; Rauk, A. *Theor. Chim. Acta* **1977**, *46*, 1−10. (b) Ziegler, T.; Rauk, A. *Inorg. Chem.* **1979**, *18*, 1755−1759. (c) Ziegler, T.; Rauk, A. *Inorg. Chem.* **1979**, *18*, 1558−1565.

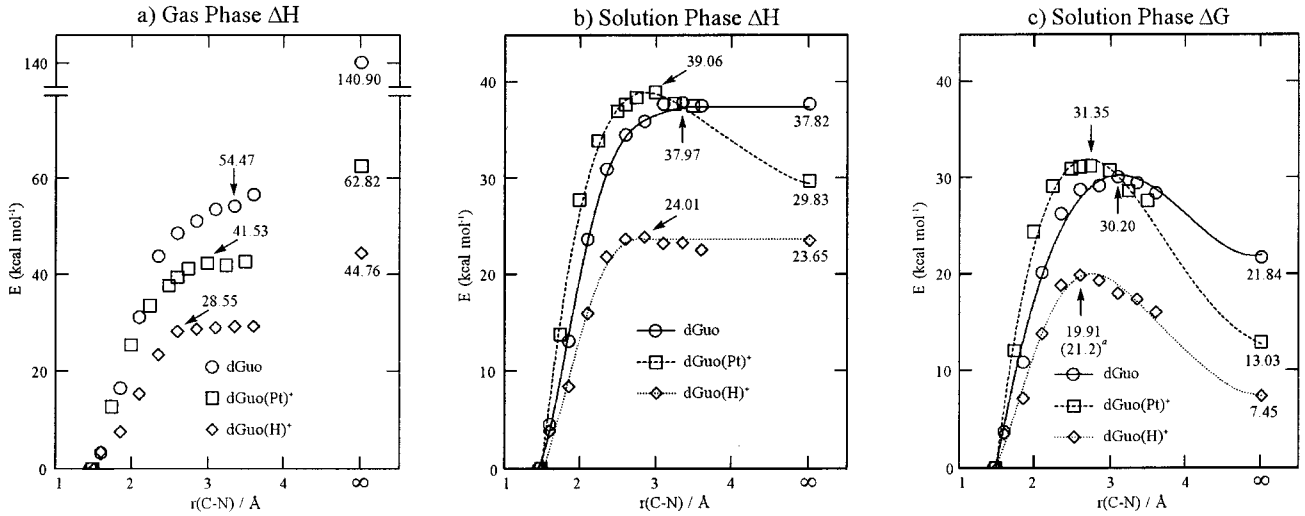

Figure 1. Reaction energy profiles (Jaguar/B3LYP/cc-pVTZ(-f)++) of dGuo, dGuo(H)$^+$, and dGuo(Pt)$^+$: (a) gas-phase enthalpies only, (b) solution-phase enthalpies, and (c) solution-phase free energies (ZPE/C_p/S corrected).

order regular approximation" (ZORA)[25] as implemented in ADF. The ADF results, which were used to provide a qualitative picture of the reactions, are complementary to the quantitative geometry optimizations, large basis set calculations, and solvation energy evaluations obtained from Jaguar.

Reaction Energy Profiles. Reaction energy profiles were computed by elongating the *N*-glycosyl bond in steps of 0.25 Å from the optimized equilibrium geometry and reoptimizing the structure with the C−N distance frozen. Attempts to find the transition state in a somewhat less arbitrary manner by using standard transition state search techniques were unsuccessful for reasons discussed in more detail below.

Entropy Corrections. The entropy corrections are simply derived from the frequency calculations for the reactant and the two products using unscaled frequencies. Note that by entropy here we refer specifically to the vibrational/rotational/translational entropy of the solute(s); the entropy of the solvent is implicitly included in the dielectric continuum model. To evaluate the entropy corrections for each sample point of the reaction energy profile, we carried out an additional frequency calculation on the data point with an elongated C−N distance of 2.8 Å for dGuo and dGuo(H)$^+$ and 2.7 Å for dGuo(Pt)$^+$. From these data point, the entropy correction at equilibrium geometry, and the sum of entropy corrections of three independent fragments d$^+$, G(H)$^-$, and G(Pt)$^-$, which serve as the asymptotic limit at infinite C−N distance, we constructed a simple interpolating exponential function of the form $f(x) = ae^{(bx)} + c$. This function computes values for the data points at any given C−N distance (Figure S3 of the Supporting Information).

Orbital Analyses. In addition to knowing the energies at the different steps along the depurination pathway, it is highly desirable to understand qualitatively how structural changes of the guanine fragment relate to the stability of the *N*-glycosyl bond. Such an understanding is best derived by identifying and examining the most important orbitals that control the electronic structure. In this study, we used two orbital analysis methods: the natural bond orbital method[23] and the fragment molecular orbital (FMO) method in combination with the extended transition state approach.[24] The NBO method represents the electronic structure close to the classical Lewis structure, by maximizing localization of otherwise diffuse molecular orbitals between the two atoms where the chemical bond is formed. Ziegler and Rauk's ETS method, on the other hand, uses unmodified canonical molecular orbitals and thus describes a bond as a complex combination of delocalized molecular orbitals. A review of both methods and their application to inorganic problems is available.[26,27] The ETS method, although widely used with the popular DFT package ADF, is somewhat less familiar than the NBO approach and is also less chemically intuitive. Therefore, we present a brief overview of the ETS method in the Supporting Information.

Results and Discussion

The foremost requirement for a successful theoretical treatment of the depurination problem is to construct reaction energy profiles that are consistent with the experimental observations described above. In recent years, DFT has been tested extensively, and it is commonly accepted that equilibrium structures can be obtained reliably by geometry optimizations at a proper level of theory. The optimized structures in our study are in good agreement with experimental observations and are given as Supporting Information. In the first part of our discussion, we present the details of the computed depurination reaction energy profiles. In the second part of the discussion, we explore electronic structure differences between G$^-$, G(H), and G(Pt) by comparing the most important molecular orbitals and the atomic charges. Lastly, N7−C1′ bond formation is examined by combining the molecular orbitals of G$^-$, G(H), and G(Pt) with those of the deoxyribose moiety.

Reaction Energy Profile. Figure 1a shows the gas-phase enthalpy profiles for the depurination reactions of dGuo, dGuo(Pt)$^+$, and dGuo(H)$^+$. In gas phase, cleavage of the C−N bond is highly endothermic for all three systems considered. Not surprisingly, heterolytic bond dissociation is most difficult for dGuo, with an overall ΔH of +140.9 kcal mol^{-1}. Both protonation and platination introduce a positive charge, which cancels the negative charge of the leaving group in dGuo. The heterolytic bond dissociation energy (BDE) decreases dramatically to +62.8 and +44.8 kcal mol^{-1} for dGuo(Pt)$^+$ and dGuo(H)$^+$, respectively. Note that BDE's are computed using the fully relaxed equilibrium structures. In good agreement with intuitive expectations, the plots in Figure 1a indicate two main

(25) (a) van Lenthe, E.; Baerends, E. J.; Snijders, J. G. *J. Chem. Phys.* **1993**, *99*, 4597−4610. (b) van Lenthe, E.; van Leeuwen, R.; Baerends, E. J.; Snijders, J. G. *Int. J. Quantum Chem.* **1996**, *57*, 281−293.

(26) Reed, A. E.; Curtiss, L. A.; Weinhold, F. *Chem. Rev.* **1988**, *88*, 899−926.
(27) Frenking, G.; Fröhlich, N. *Chem. Rev.* **2000**, *100*, 717−774.

effects determining the shape of the fragmentation energy profile. At the beginning of the bond elongation process, the main force that needs to be overcome is the electronic bond strength of the N9−C1′ bond. At a N9−C1′ distance of approximately 2.7 Å, the *N*-glycosyl bond is nearly broken. Further increase of the N−C distance gives only a small change in energy indicated by a plateau at approximately 55, 42, and 29 kcal mol^{-1} for dGuo, dGuo(Pt)$^+$, and dGuo(H)$^+$, respectively. To complete the process, electrostatic forces holding the fragments together must be overcome. These forces are substantially larger for the cation−anion ion pair [d$^+$]−[G$^-$] than for the cation−neutral pairs [d$^+$]−[G(Pt)] and [d$^+$]−[G(H)]. The reaction energy profiles in Figure 1a indicate that an additional 86, 21, and 16 kcal mol^{-1} are necessary, respectively, to complete the separation after the energy plateau is reached. These gas-phase energy profiles are, however, misleading when used as an indicator for the stability of the glycosyl bond in solution. The depurination of dGuo, which generates two charged species from a neutral reactant, has substantially greater stabilization of the products due to solvation than the reactions of dGuo(Pt)$^+$ and dGuo(H)$^+$ in which cationic and neutral fragments are formed from an originally cationic molecule. The addition of solvation corrections changes the BDE's by 25.8 and 19.5 kcal mol^{-1} to 37.0 and 25.3 kcal mol^{-1} for dGuo(Pt)$^+$ and dGuo(H)$^+$, respectively, whereas a shift of 101.6 kcal mol^{-1} to give a BDE of +39.2 kcal mol^{-1} is computed for dGuo. The solvation corrected energy profiles are shown in Figure 1b. Unlike the gas-phase BDE's, which indicated substantially different reaction energy profiles for the three systems, the solution-phase calculations give more comparable results. A comparison of the gas-phase and solution profiles illustrates clearly how solvation compensates for the long-range electrostatic attraction that made the separation of the fragment ion pairs a thermodynamically uphill process in the gas phase. In the case of dGuo(Pt)$^+$, the solvation energy is larger than the electrostatic ion pairing energy, such that the energy profile shows a favorable ion pair dissociation. By comparison, the solvation corrections for the early part of the reaction energy profiles are small. The N−C bond cleavage requires approximately 38, 39, and 24 kcal mol^{-1} for dGuo, dGuo(Pt)$^+$, and dGuo(H)$^+$, respectively.

The last important corrections to be considered are the changes of the zero-point energy, heat capacity (C_p), and entropy (S) upon fragmentation. The fragmentation of the single reactant molecule into two products is entropically favorable. Addition of the ZPE/C_p/S corrections gives reaction free energy profiles, shown in Figure 1c. The final reaction free energy of the depurination reaction is 21.8, 13.0, and 7.5 kcal mol^{-1} for dGuo, dGuo(Pt)$^+$, and dGuo(H)$^+$, respectively. This trend is in good agreement with the expectation that addition of the [Pt] group should make the guanine fragment a better leaving group than G$^-$. The overall reaction energy is 8.8 kcal mol^{-1} less uphill. As Figure 1c illustrates, however, the depurination of dGuo and dGuo(Pt)$^+$ share the same kinetic barrier of approximately 30 kcal mol^{-1}, whereas the barrier is only 20 kcal mol^{-1} for dGuo(H)$^+$. The latter compares favorably with the experimental activation free energy of 21.2 kcal mol^{-1} for acid-catalyzed hydrolysis of dGuo.[6a]

Figure 1 demonstrates that a well-defined transition state can only be located reliably in the free energy space, making it impossible to locate such a transition state using standard techniques that only sample the enthalpic potential energy surface. Computation of the exact transition state and its energy, however, is not necessary to understand the relative kinetic stability of the C−N bond in dGuo(Pt)$^+$. Although the gas-phase enthalpy profiles do not indicate a transition state for the reaction, the energetic plateaus on the potential energy surface can be used to examine the main electronic features determining the height of these plateaus. The energy required to reach this point on the potential energy surface is mainly determined by the electronic energy needed to break the C−N bond. Thus, although the consideration of solvation and entropy changes are crucial for modeling the depurination reaction realistically, the key to understanding the qualitatively different influence of H$^+$ and *cis*-[Pt(NH$_3$)$_2$Cl]$^+$ fragments on the stability of the glycosyl bond lies in the details of electronic structure changes that determine the height of the energy plateau seen in Figure 1a. The goal of the following analysis, therefore, is to examine the electronic features leading to the higher plateau energy for dGuo(Pt)$^+$ compared to dGuo(H)$^+$. Below, we first discuss the electronic structure of the fragments G(Pt) and G(H), followed by an analysis of the bonding between the cationic deoxyribose based oxocarbenium fragment and the three guanine-based fragments G$^-$, G(Pt), and G(H), respectively. It is also useful to analyze the charge distribution in the molecular building blocks and the charge reorganization upon bond formation, which provide an overall picture of the orbital reorganization (see Supporting Information).

MO Diagrams. The expression of molecular orbitals as linear combinations of atomic orbitals (LCAO) often gives rise to a complicated description for systems containing more than a few atoms. One method of simplifying the orbital analysis and identifying relevant interactions for a particular chemical bond is to carry out fragment calculations, where the molecule is divided into chemically intuitive building blocks. Once the wave functions for the molecular fragments are obtained in separate calculations, the fragment molecular orbitals (FMO) are used instead of atomic orbitals to form the linear combinations. The MO diagram shown in Figure 2 compares the molecular orbitals of cisplatin with those of the [Pt]$^+$ fragment; only MO's with significant metal character are drawn. As expected for a 16e$^-$ Pt(II) d^8 system, the LUMO of cisplatin is a σ-antibonding orbital, MO-⟨24⟩, with significant metal $d_{x^2-y^2}$ character. The four occupied metal d-based MO's can easily be identified as the highest energy orbitals ⟨19⟩−⟨23⟩. The metal−ligand bonding orbitals are also shown in Figure 2. The energy mismatch of the NH$_3$ and Cl$^-$ ligand orbitals results in splitting of the expected a_2-type σ-orbital (assuming local symmetry of C_{2v}) with in-phase combinations along all four σ-bond axes. Instead, there are two MO's, ⟨13⟩ and ⟨15⟩, each with pairwise in-phase combinations between Pt−Cl and Pt−N bonds, respectively. Removal of one chloride ligand affords a 14e$^-$ species, [Pt]$^+$, with two empty metal d-based MO's. As Figure 2 demonstrates, substantial reorganization takes place after ligand dissociation. Interestingly, the LUMO of the [Pt]$^+$ is very similar to the LUMO of cisplatin with σ-antibonding combinations between Pt $d_{x^2-y^2}$ and the p-orbitals of the remaining ligands. The new empty Pt d-based MO-⟨22⟩ is significantly higher in energy and is best described as a d_{y^2}-based orbital[28] with strong antibonding character along the Pt−Cl and the Pt−N bond trans to the

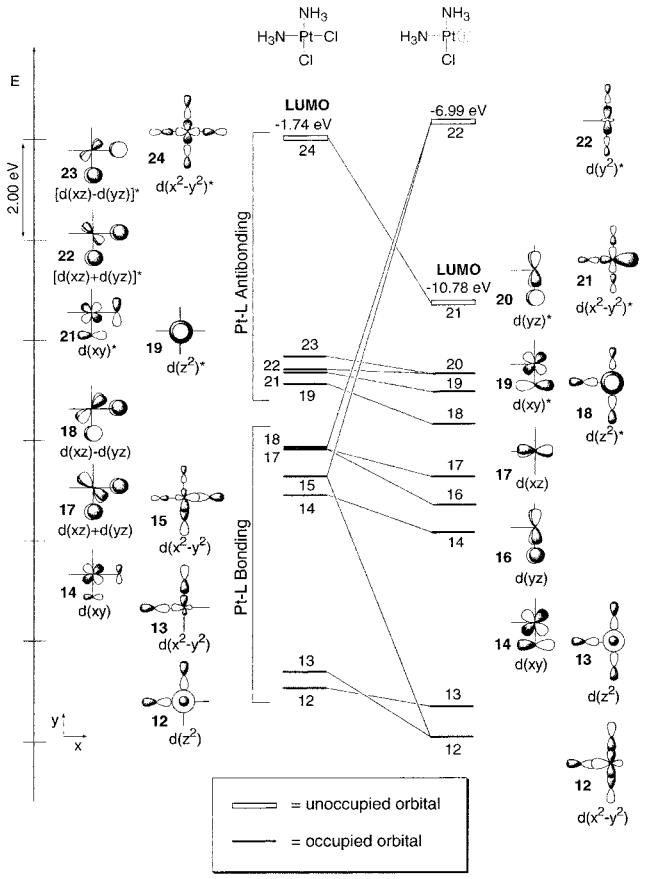

Figure 2. Schematic correlation of molecular orbitals of *cis*-$[Pt(NH_3)_2(Cl)_2]$ and *cis*-$[Pt(NH_3)_2(Cl)]^+$. Energy scales have been shifted for the convenience of drawing.

remaining chloride ligand. Most important for the forthcoming analysis is that the σ-bonding between Pt and the leaving group in cisplatin is originally promoted through MO-$\langle 15\rangle$, which, after chloride dissociation, becomes after some mixing with MO-$\langle 13\rangle$ the new molecular orbital $[Pt]^+$-$\langle 12\rangle$. Note, that $[Pt]^+$-$\langle 12\rangle$ resembles the 4-fold in-phase combination, an a_2-type orbital in a C_{2v} environment with matching ligand orbitals, that would usually be anticipated as the lowest energy bonding orbital.

The next step in our molecular building block approach is shown in Figure 3.[29] The orbital interaction of the empty 1s orbital of $[H]^+$ with the G^- FMO's is shown on the right-hand side of Figure 3 and is easily understood. Only two G^--based fragment orbitals, G^--$\langle 14\rangle$ and G^--$\langle 27\rangle$, overlap strongly enough with the empty 1s orbital of the $[H]^+$ fragment to contribute significantly to proton binding (Table S4, Supporting Information). The contour plots shown in Figure 4a illustrate the spatial distribution of these two orbitals. Both G^--$\langle 14\rangle$ and G^--$\langle 27\rangle$ are orbitals showing maximum electron density at N7 and N9, where G^--$\langle 14\rangle$ is a σ-orbital with substantial delocalization into the six-membered ring. G^--$\langle 27\rangle$ is also a σ-orbital but is much more localized on the five-membered ring and has a node that bisects this ring horizontally. Note that sp hybrid fragment orbitals on N7 and N9 are out-of-phase with each other. The in-phase combination, G^--$\langle 25\rangle$, is 0.47 eV lower in energy and has less lone-pair character on the nitrogen atoms. The molecular orbitals with largest N−[H] σ-character, G(H)-$\langle 10\rangle$/G(H)-$\langle 15\rangle$ are schematically depicted in Figure 3 and their contour plots shown in Figure 5a,b. These two molecular orbitals capture essentially all of the $[H]^+/G^-$ interactions. G(H)-$\langle 10\rangle$ is mainly a combination of -[G^--$\langle 14\rangle$] and +[H^+-1s], giving rise to two nodes in the five-membered ring as shown in Figure 5a and substantial s-orbital character at the N9 position as a result of dehybridization. The second N7−H σ-bonding orbital, G(H)-$\langle 15\rangle$, can be envisioned as the σ combination with an additional node that lies along the midpoint of the N7−C5 bond and N9. It is crucial to note that this orbital introduces a node at N9. Since the electron density donation upon N9−C1′ bond formation will occur along the N9−C1′ vector, changes to orbitals that are approximately orthogonal to the N9−C1′ vector, such as the G(H)-$\langle 15\rangle$, have no direct effect to the N9−C1′ bonding. This detailed picture is not in complete agreement with the simplest "back-of-an-envelope" approximation. If only the highest occupied σ-orbital of the G^--fragment, G^--$\langle 27\rangle$, and the lowest unoccupied $[H]^+$ 1s orbital are considered for bonding, one would sketch the molecular orbital G(H)-$\langle 15\rangle$, which is an in-phase combination of the two frontier orbitals. Our analysis shows, however, that the involvement of one of the lower-lying G^--fragment orbitals, G^--$\langle 14\rangle$, is crucial. It is the main contributor to the G−H bonding orbitals G(H)-$\langle 10\rangle$ (31%) and G(H)-$\langle 15\rangle$ (62%). In comparison, the frontier orbital G^--$\langle 27\rangle$ plays only a minor role with contributions around 13 and 11%, respectively, to the bonding orbitals.

The molecular orbital diagram of G(Pt) is more challenging to understand. First of all, the metal d orbitals can interact with the π-orbitals of the guanine ring. Since the bound [Pt] fragment shows low local symmetry due to the dihedral angle of approximately 45°, substantial mixing of metal d-based fragment orbitals is expected. Indeed, we can easily identify at least four molecular orbitals G(Pt)-$\langle 35\rangle$, G(Pt)-$\langle 38\rangle$, G(Pt)-$\langle 45\rangle$ and G(Pt)-$\langle 46\rangle$ with substantial metal d- and G^--fragment orbital characters. These interactions are depicted schematically on the left-hand side of the simplified MO diagram (Figure 3). They play an important role in the redistribution of electron density upon platination, thereby influencing the overall reactivity of G(Pt). No evidence of direct electronic involvement of these interactions in dictating the stability of the *N*-glycosyl bond is found, however. Therefore, other than displaying the energies of these orbitals in the MO diagram, which is helpful in contrasting the qualitatively different electronic structures of G(H) and G(Pt), they are not further discussed. More relevant to the objective

(28) MO-$\langle 22\rangle$ is an admixture of $d_{x^2-y^2}$ and d_{z^2} orbitals in addition to Pt s and Pt p_x orbitals generating an orbital that essentially lies along the *y*-axis. If the six second-order Cartesian d functions d_{x^2}, d_{y^2}, d_{z^2}, d_{xy}, d_{xz}, and d_{xz} are used instead of the conventional five d-orbital basis to describe the same molecular orbital, the domination of the d_{y^2} character becomes more apparent, which is also illustrated by the shape of the isodensity surface of this MO (see Supporting Information Figure S8).

(29) If the fragments carry different charges, an additional complication for the MO diagram arises from shifts of all fragment orbital energies due to electrostatic forces that readjust upon bond formation. To obtain MO diagrams that provide a qualitatively insightful picture, it is necessary to shift the energy scales according to an 'internal reference'. Figure 3 shows a schematic MO diagram derived from the ADF fragment calculations comparing the interactions of the cationic $[Pt]^+$ and $[H]^+$ fragment orbitals with those from the anionic G^- fragment to give the neutral product. A convenient energy reference relating the orbital energies of G^- and the G(Pt) fragments is the π-type HOMO, G^--$\langle 28\rangle$, which essentially forms the HOMO of G(Pt) with a contribution of 90.2%, whereas [Pt]-based orbitals contribute less than 5%. Thus, the orbital energy scales of the neutral and anionic systems have been shifted to give the horizontal correlation line for the MO's G^--$\langle 28\rangle$ and G(Pt)-$\langle 48\rangle$. Similarly, the FMO $[Pt]^+$-$\langle 20\rangle$, which is a π*-type orbital between the Pt d_{yz} orbital and one of the Cl p orbitals, accounts for 95.7% of the MO G(Pt)-$\langle 47\rangle$. These two orbitals have been used as anchor points of the cationic and neutral fragment orbitals. Both $[H]^+$- and G(H)-based orbitals are drawn on the same energy scale as $[Pt]^+$ and G(Pt), respectively, to allow cross-referencing.

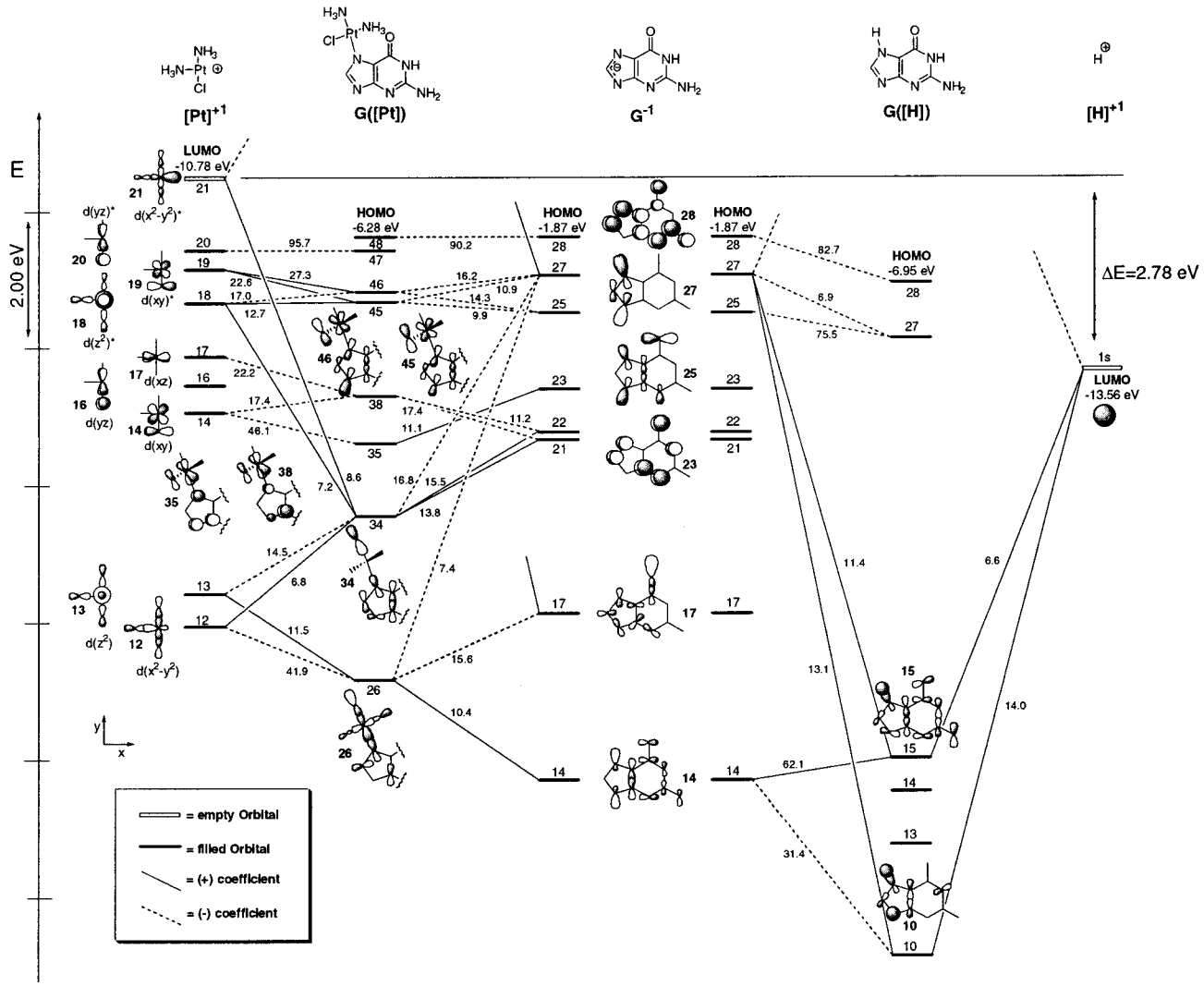

Figure 3. Simplified partial MO diagrams of G(Pt) and G(H) using the fragment orbitals of G^-, *cis*-$[Pt(NH_3)_2(Cl)]^+$, and H^+ as building blocks. Cartoon representations of selected orbitals are drawn. In the cartoons, the main atomic orbital characters of the MO's are exaggerated.

of this study are the σ-type interactions between $[Pt]^+$ and the G^- fragments. The MO diagram identifies two important MO's arising from interactions of the fragment orbitals with the proper symmetry to form σ-bonds, G(Pt)-$\langle 26\rangle$ and G(Pt)-$\langle 34\rangle$. Unlike in the simple proton case where only the empty 1s orbital was considered, there are four $[Pt]^+$ fragment orbitals that can interact with the in-plane σ-orbitals of the G^- fragment: $[Pt]^+$-$\langle 21\rangle$, $[Pt]^+$-$\langle 18\rangle$, $[Pt]^+$-$\langle 13\rangle$, and $[Pt]^+$-$\langle 12\rangle$. These are essentially the metal−ligand bonding and antibonding combinations of the Pt d_{z^2} and Pt $d_{x^2-y^2}$ orbitals. Not surprisingly, most important for the N−Pt bonding are the two fragment orbitals, $[Pt]^+$-$\langle 21\rangle$ and $[Pt]^+$-$\langle 12\rangle$, derived from Pt $d_{x^2-y^2}$, which are shown in Figure 4b as contour plots. A further complication is the participation of another ring σ-orbital (G^--$\langle 17\rangle$), which shows nonnegligible overlap with Pt-based orbitals (Table S4, Supporting Information), in the [Pt]−G bonding to form the N−Pt bonding orbital G(Pt)-$\langle 26\rangle$ and the orbital G(Pt)-$\langle 34\rangle$. The contour plots of both orbitals are shown in Figure 5c,d. Comparing G(Pt)-$\langle 26\rangle$ with both G(H)-$\langle 10\rangle$ and G(H)-$\langle 15\rangle$, we can clearly see that G(Pt)-$\langle 26\rangle$ corresponds to G(H)-$\langle 15\rangle$. Both show in-phase overlap between C4 and C5 and a vertical node bisecting the five-membered ring. G(H)-$\langle 10\rangle$ also shows an in-phase overlap between C4 and C5, but lacks the additional vertical node. As the contour plot in Figure 5d reveals, the complicated mixing of the four $[Pt]^+$-based orbitals seen in the MO diagram for the formation of G(Pt)-$\langle 34\rangle$ (6.8% $[Pt]^+$-$\langle 12\rangle$, 14.5% $[Pt]^+$-$\langle 13\rangle$, 7.2% $[Pt]^+$-$\langle 18\rangle$, 8.6% $[Pt]^+$-$\langle 21\rangle$) affords effectively the complete removal of metal d character, leaving an amplified contribution from the NH_3 p orbital with some metal p contribution. Formally, this orbital is the out-of-phase combination of the Pt $d_{x^2-y^2}$ dominated N−Pt bonding orbital G(Pt)-$\langle 26\rangle$. By diminishing the metal $d_{x^2-y^2}$ character of this formally Pt−N7 antibonding orbital and directing the electron density to the NH_3 ligand away from the N−Pt bond, the originally ineffective filled−filled interaction of the fragment orbitals $[Pt]^+$-$\langle 12\rangle$ and the guanine-ring σ-orbitals, which would have afforded one bonding and one antibonding orbital, is avoided. The most important feature is that both orbitals involving G−[Pt] interactions that ultimately dictate the pathway for electron withdrawal from the guanine ring to the [Pt] fragment introduce a node at N9, thereby allowing electron density deformation that minimally impacts the N9−C1′ bond.

Thus, the G−[Pt]/[H] bonds are only partially comparable. The N7−Pt/H bonding in both cases is promoted through an N7−Pt/H in-phase combination of G^--$\langle 14\rangle$ with the $[H]^+$-1s and $[Pt]^+$-$\langle 12\rangle$, where only N7−H qualifies as a classical donor−

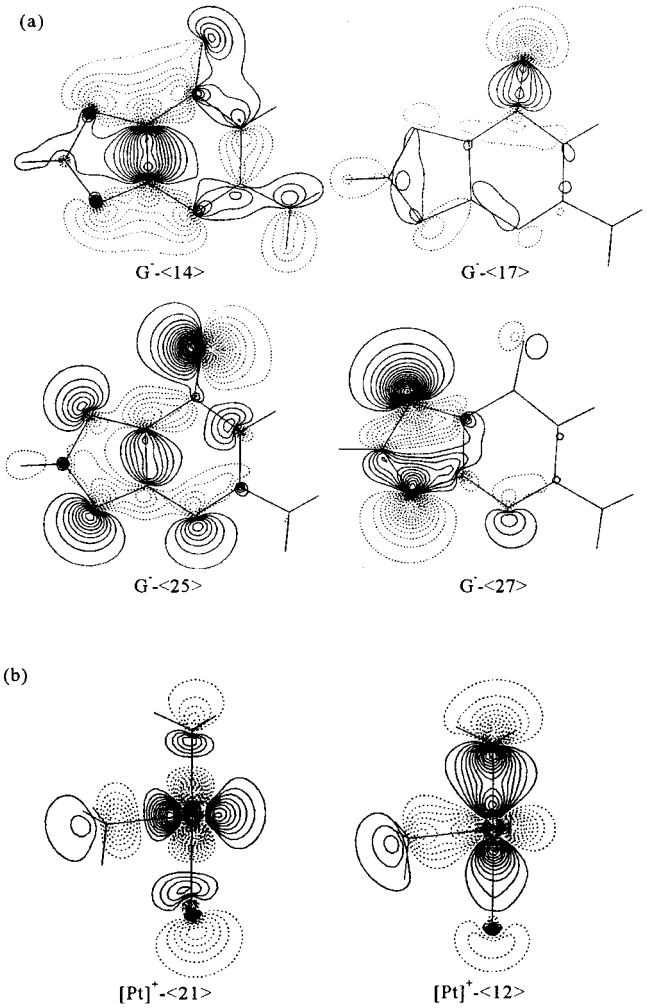

Figure 4. Contour plots (contour interval: 0.025 au) of the most important orbitals: (a) G^--based-fragment orbitals; (b) $[Pt]^+$-based-fragment orbitals.

acceptor bond. The N7−Pt bond is better characterized as a filled−filled interaction with an orbital relaxation pattern that reduces the antibonding interaction, giving a net bonding interaction. The empty fragment orbital $[Pt]^+$-⟨21⟩ does not fully participate in bonding as parts c and d of Figure 5 show, but directs an efficient orbital reorganization that diminishes the N−Pt antibonding interaction. For the strongly N−H bonding orbital G(H)-⟨10⟩, which is the lowest energy bonding combination of the overall three-orbital, four-electron combination (G^--⟨14⟩, G^--⟨27⟩, H^+-⟨1s⟩), no corresponding molecular orbital can be found in G(Pt). As shown in the contour plot of G(H)-⟨10⟩ (Figure 5a), electron density around N9 is directly involved in the N7−H σ-bonding orbital, giving rise to an efficient pathway for σ-electron density removal from N9 upon protonation at the N7 position.

***N*-Glycosyl Bond Formation.** The N9−C1′ bond formation between the deoxyribose and guanine fragments adds another level of complexity to the corresponding MO diagram as compared to that shown for G(Pt) in Figure 3, since another asymmetric fragment (d^+) enters the scene. Beside the most important donor−acceptor interactions between the filled σ-orbitals of the guanine ring and the LUMO of the sugar moiety, substantial reorganization of the guanine π-orbitals is present. After much effort to obtain an intuitive MO diagram comparable to that shown in Figure 3, we have concluded that the

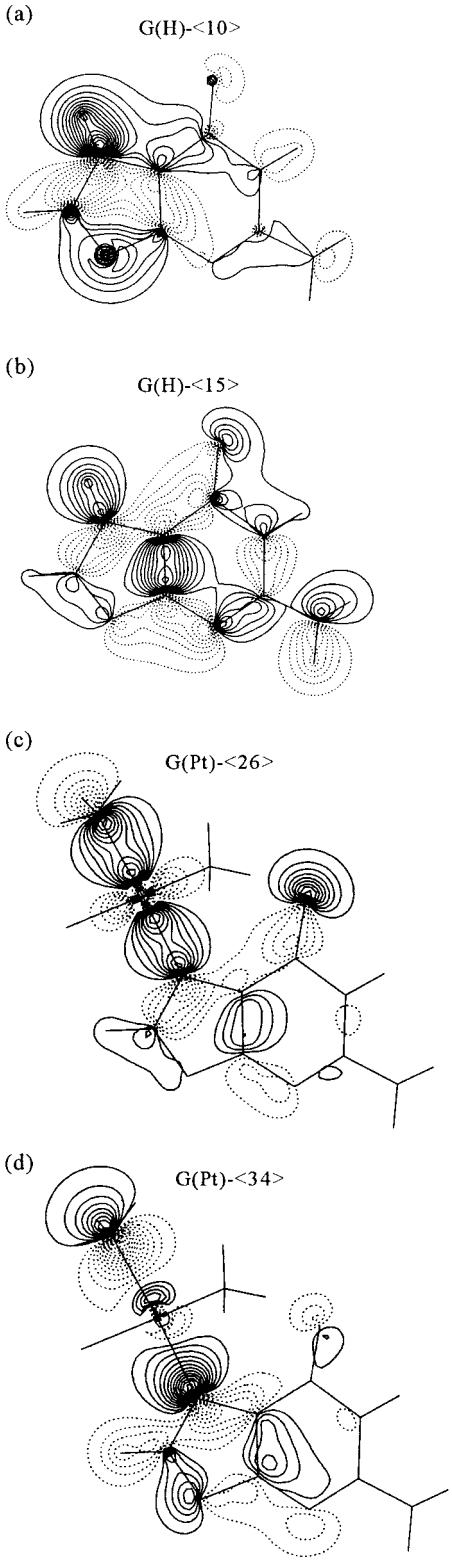

Figure 5. Contour plots of the most important molecular orbitals.

complexity of the MO diagram with severely delocalized orbitals adds little insight to the bonding of d−G(Pt/H). A different approach was therefore adopted to simplify the analysis.

Orbital Analyses. Table 1a gives the energy decomposition for dGuo, $dGuo(Pt)^+$, $dGuo(H)^+$ and the energy difference between $dGuo(Pt)^+$ and $dGuo(H)^+$ according to the ZR scheme.[24] The ADF and Jaguar results for the overall bond dissociation energies are in fair agreement. Most importantly, both gas-phase

Table 1.

	dGuo	dGuo(Pt)$^+$	dGuo(H)$^+$	dGuo(H)$^+$–dGuo(Pt)$^+$
(a) Ziegler−Rauk Energy Decomposition[a]				
kinetic	1341.96	1272.47	1221.72	
coulombic	726.82	713.19	676.20	
LDA-XC (Xα)	239.22	229.00	220.37	
exchange (B)	26.64	29.14	26.96	
correlation (LYP)	20.06	20.75	19.59	
total ΔE_{Pauli}	**382.50**	**338.65**	**332.52**	**6.13**
total $\Delta E_{\text{el-st.}}$	**278.80**	**194.08**	**178.34**	**15.74**
total $\Delta E_{\text{orb-int}}$	**313.16**	**259.48**	**249.64**	**9.84**
total ΔE_{int}	**209.46**	**114.91**	**95.46**	**19.45**
ΔE_{prep}[b]	56.44	56.44	56.44	
total bonding energy (ADF)	153.02	58.47	39.02	
ratio $\Delta E_{\text{orb-int}}/\Delta E_{\text{el-st.}}$	1.12	1.34	1.40	
total bonding energy[c]	144.77	69.09	50.52	
(b) NBO Analysis for the N9−C1′ Bond Orbital[c]				
Wiberg bond Index, *P*	0.930	0.884	0.850	
N9 AO, %	**63.68**	**65.58**	**66.48**	
N9 2s, %	34.15	34.14	33.63	
N9 2p, %	65.81	65.83	66.34	
C1 AO, %	**36.32**	**34.42**	**33.52**	
C1 2s, %	23.50	21.39	20.16	
C1 2p, %	76.36	78.45	79.67	

[a] Using the fragments d^+ and G^-/G(Pt/H). Energies are given in kilocalories per mole. [b] ΔEprep is essentially the energy difference between the free oxocarbenium ion with a planar conformation around C1′ and the sugar conformation found in guanosine (Figure S1, Supporting Information). The structural change of the G(Pt/H) moiety is negligibly small and has been omitted for simplicity. [c] Jaguar/B3LYP/LACVP**.

results indicate that the N9−C1′ bond is 19 kcal mol^{-1} stronger in dGuo(Pt)$^+$ than in dGuo(H)$^+$. The most useful feature of the ZR method, the separate evaluation of the orbital interaction energies according to their symmetry, is not available in this case due to the intrinsic lack of symmetry. However, the ZR scheme also provides a measure for the ionic and covalent character of the bond by evaluating the electrostatic and the orbital interaction terms between the molecular fragments separately.[30,31] In dGuo, the electrostatic contribution to the total bond energy is −278.8 kcal mol^{-1}, whereas −313.2 kcal mol^{-1} is computed for the orbital interaction term, giving a fairly balanced covalent/ionic ratio of 1.12. Given the donor−acceptor character of the *N*-glycosyl bond, the intuitive expectation is that the depletion of electron density at N9 should have a larger effect on the electrostatic part of the bond energy. The results of the ZR analysis listed in Table 1a confirm this expectation. The electrostatic contribution to the bond energy in dGuo(Pt)$^+$ is −194.1 kcal mol^{-1}, whereas −178.3 kcal mol^{-1} is computed for dGuo(H)$^+$. Interestingly, the orbital interaction part also decreases notably from −259.5 to −249.6 kcal mol^{-1}. The initial $\Delta E_{\text{orb-int}}/\Delta E_{\text{el-st}}$ ratio for dGuo of 1.12 increases to 1.34 and 1.40 for dGuo(Pt)$^+$ and dGuo(H)$^+$, respectively. This result means that, whereas the absolute bond order decreases in the series of dGuo, dGuo(Pt)$^+$, and dGuo(H)$^+$, the *N*-glycosyl bond becomes increasingly more covalent. The electrostatic term decreases in a more pronounced manner than the orbital interaction term, which is the basis for covalent bonding. The simplest and most natural picture of the glycosyl bond is that of a filled sp^2-hybridized lone pair at N9 donating electron density to an empty sp^3-hybrid orbital centered at C1′ (Figure S6, Supporting Information). This localized picture is not appropriate for understanding the details of bonding, because substantial orbital reorganization takes place and lower lying orbitals of appropriate symmetry contribute substantially. In fact, such a simple picture would a priori fail to recognize the control mechanisms by long-range orbital mixing outlined above. The

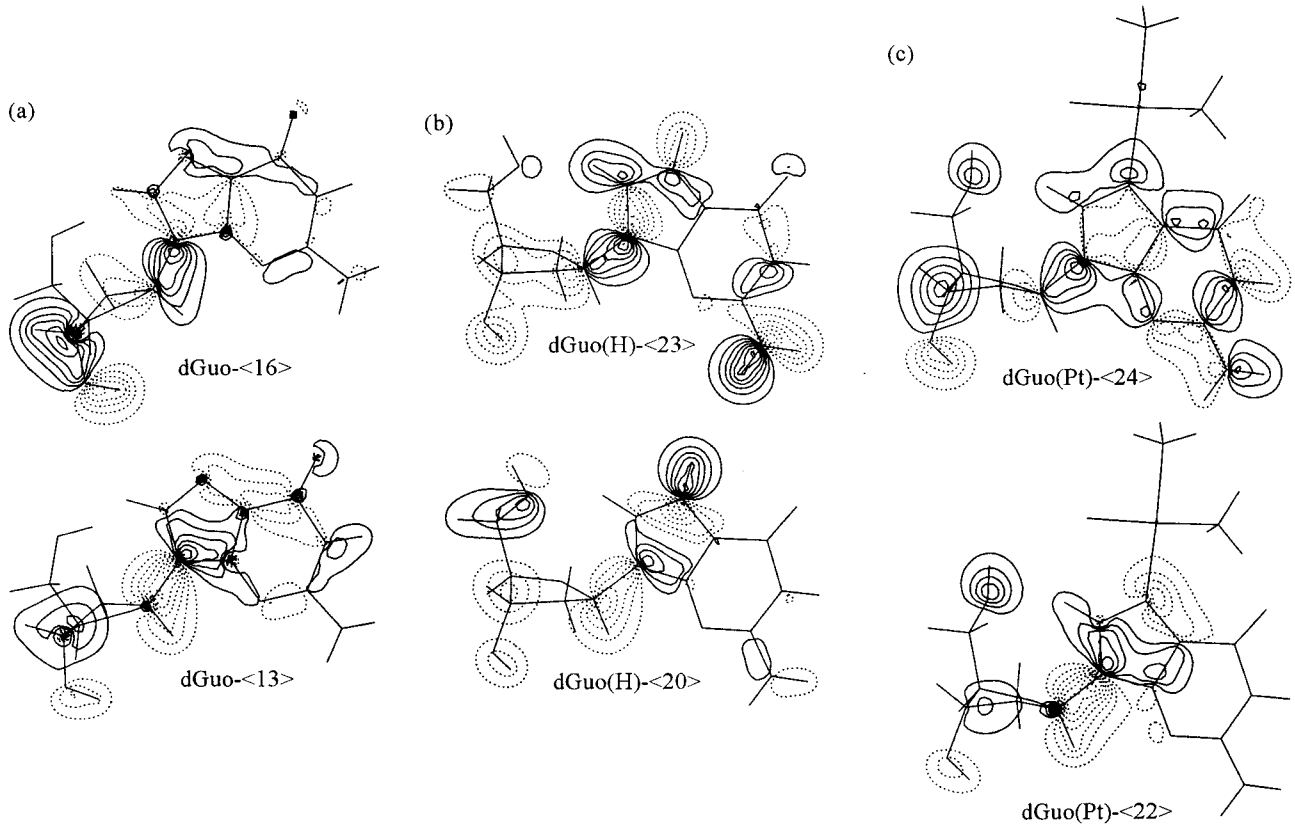

Figure 6. Contour plots (contour interval: 0.025 au) of the most important orbitals for the *N*-glycosyl bond: (a) in dGuo; (b) dGuo(H)$^+$; (c) dGuo(Pt)$^+$.

NBO analysis provides an appropriate transform of the delocalized orbitals to localized ones while integrating these long-range effects into the final form of the localized bond orbitals. The NBO results for the N9−C1′ bond are summarized in Table 1b. In good agreement with the picture emerging from the ZR analysis, the Wiberg bond index *P* for these three systems decreases from 0.930 in dGuo to 0.884 in dGuo(Pt)$^+$ and 0.850 in dGuo(H)$^+$, again indicating more pronounced destabilization upon [H]$^+$ addition compared to that of [Pt]$^+$. Two of the most important canonical orbitals promoting N9−C1′ for each of the three systems are shown in Figure 6 as contour plots. After orbital localization the natural bond orbital, a linear combination of carbon and nitrogen centered sp-hybrid orbitals (Figure S7, Supporting Information) is obtained. The composition of the natural bond orbitals, listed in Table 1b, shows a systematic trend. The nitrogen atom orbital character increases systematically from 63.7 to 65.6 and 66.5% for dGuo, dGuo(Pt)$^+$, and dGuo(H)$^+$, respectively. Also, a systematic increase of the p-orbital character in both carbon- and nitrogen-based sp-hybrid orbitals is observed. Thus, an alternative way of rationalizing the loss of N9−C1′ bond strength in the series of dGuo, dGuo(Pt)$^+$, and dGuo(H)$^+$ is the increasing loss of s-character of the sp-hybrid orbital forming the σ-bond as a result of stronger involvement of the N9 2s orbital in the formation of the N7−H bonding orbital (Figure 5a).

Conclusions

We have computed the depurination reaction free energy profiles for guanosine and the N7-protonated and N7-platinated analogues dGuo(H)$^+$ and dGuo(Pt)$^+$ in solution. The main findings of this work are as follows:

(1) For all three systems, the transition state can only be located in the solution-phase free energy space. Both solvation and entropy corrections are equally important in obtaining a realistic model.

(2) In good agreement with experimental observations, our calculations indicate that protonation gives rise to a substantial acceleration of the depurination reaction by decreasing the transition-state energy by ∼10 kcal mol^{-1}.

(3) N7-platination also lowers the total free energy for the reaction significantly, but the kinetic barrier for the bond rupture is essentially the same in dGuo and dGuo(Pt)$^+$. This result explains the lack of the destabilizing effect observed in experiments.

(4) Detailed orbital analyses reveal that the relative barrier height of the transition state is determined by the electronic contributions to the N9−C1′ bond strength. Poor overlap of the [Pt] LUMO, a Pt($d_{x^2-y^2}$) ligand σ-antibonding orbital, and the presence of lower lying metal d-orbital-based fragment orbitals, the Pt($d_{x^2-y^2}$) ligand σ-bonding orbital in particular, afford a very different orbital interaction pattern for dGuo(Pt)$^+$ than dGuo(H)$^+$. The former involves electron-density withdrawal from an orbital with a node at the N9 position that leaves the N9 electron density along the N9−C1′ axis essentially intact. As a result, the N9−C1′ bond in dGuo(Pt)$^+$ resembles that in dGuo more closely than it does the corresponding bond in dGuo(H)$^+$, giving rise to a similar short-range energetics for dGuo and dGuo(Pt)$^+$ with respect to N9−C1′ bond elongation.

(5) The ESP fit atomic charge analysis (see Supporting Information) indicates notably different charge dissipation patterns induced by the proton and the [Pt]$^+$ moieties. Whereas protonation leads to a more local charge polarization at the five-membered ring, the calculations suggest a larger charge polarization in the six-membered ring of the guanine fragment upon platination, which may have a substantial effect on base pairing and the structure of the DNA duplex.[32]

Acknowledgment. This work was supported by grants from the NIH to R.A.F. (GM 40526) and to S.J.L. (CA 34992). Computational resources were provided by the NPACI program under a grant to R.A.F. and by NCRR division of NIH (P41 RR06892). We thank Professor Cynthia K. Schauer for kindly providing access to ADF. S.J.L. acknowledges a stimulating discussion with Professor Albert Eschenmoser that helped to inspire this study.

Supporting Information Available: Additional discussions on SCRF calculations, ETS method, optimized structures, alternative site for initial protonation, entropy corrections, ESP fit atomic charges, calculated vibrational frequencies of all systems (PDF). This material is available free of charge via the Internet at http://pubs.acs.org.

JA017588+

(30) Uddin, J.; Frenking, G. *J. Am. Chem. Soc.* **2001**, *123*, 1683−1693.
(31) See Supporting Information for a more detailed explanation.
(32) (a) Burda, J. V.; Sponer, J.; Leszczynski, *J. Phys. Chem. Chem. Phys.* **2001**, *3*, 4404−4411. (b) Sigel, R. K. O.; Lippert, B. *Chem. Commun.* **1999**, *21*, 2167−2168.